Practical Analysis and Design of a 50:1 Cycloidal Magnetic Gear with Balanced Off-Axis Moments and a High Specific Torque for Lunar Robots

Bryton Praslicka*, Matthew Johnson**, Daniel Zamarron*, Avery Marshall***, Shima Hasanpour*, Matthew C. Gardner[†]
Alex Nguyen[‡], Abas Goodarzi[‡], Enzo Bauk[‡], Hamid A. Toliyat*
Email: bryton.praslicka@tamu.edu
*Department of Electrical and Computer Engineering, Texas A&M University, College Station, TX, USA
**U.S. Army Research Laboratory, U. S. Army CCDC, College Station, TX, USA
***Department of Mechanical Engineering, Texas A&M University, College Station, TX, USA
[†]Department of Electrical and Computer Engineering, University of Texas at Dallas, Richardson, TX, USA
[‡]US Hybrid Corporation, Torrence, CA, USA

Abstract—Future space missions require new robotic technologies, such as precision gearboxes capable of achieving speed-reduction ratios in excess of 1000:1, specific torques exceeding 50 N*m/kg, operation in environmental temperatures as low as 40 K, and operation in low-atmosphere or hard vacuum, with high reliability and lifetime. The tribological challenges associated with lengthy missions in harsh space environments may be ameliorated with contactless magnetic gearing solutions. This paper employs an extensive parametric 2-D finite element analysis (FEA) study to optimize the high-torque stage of a two-stage surface permanent magnet radial flux cycloidal magnetic gear train, accounting for the impacts of practical fabrication constraints, which degrade the achievable performance and shift the optimal gear ratio. This paper presents a novel discussion of the internal stress distribution and the reaction forces acting on the structure of the cycloidal magnetic gear. This paper also proposes a rotor with three sections to simultaneously balance the center of mass, radial magnetic forces, and off-axis torques. A proof-of-concept prototype was developed, and the experimental slip torque and specific torque are presented. The specific torque of the prototype discussed in this paper is competitive with commercial mechanical cycloidal-type drives with a similar torque rating.

Keywords—*Bearing loss, cycloidal magnetic gear, finite element analysis (FEA), reaction forces, stress distribution, gear ratio, magnetic gear, optimization, space, specific torque, torque density*

I. INTRODUCTION

NASA's future space exploration goals require significant advances in extra-terrestrial rover traction and actuation technologies. Harmonic drives are advantageous for low power, limited life applications, but their high sliding and wear significantly limit their suitability for high-power, long-life applications [1]. The 80:1 harmonic-type speed reducers for the Apollo 17 lunar rover traction drive [2] and two-stage planetary gearhead-harmonic drive speed reducers used in the joints of the Mars Surveyor '01 Lander robotic shoulder elevation actuator

[3] used heaters to warm the grease of the drive system when necessary to the nominal minimum operating temperature of at least 208 K (-65°C). The environments of future rover missions to permanently cratered regions of the lunar South pole, where water ice is most likely to be found, are harsh, dusty, and extremely cold (<-260°C); additional heating or advanced technologies to withstand the environment will be required [1]. However, even with advanced materials such as bulk metallic glass (BMG) and dry-film lubrication, such as moly (MoS_2), there may be insurmountable tribological challenges associated with tooth meshing or rolling in mechanical gears with high gear ratios at such low temperatures [4].

Magnetic gearboxes perform the same function as mechanical gearboxes but use modulated magnetic fields, instead of interlocking teeth, to transfer power. This noncontact power transmission offers the potential for significant lifetime and range extension, amelioration of lubrication challenges, acoustic noise reduction, and physical isolation of shafts. NASA has already begun to explore magnetic gearing solutions for aerospace actuation [5] and electric aircraft propulsion [6], and other researchers have demonstrated their operation at low temperatures for space applications [7], [8]. Beyond cryogenic applications, magnetic gearboxes and integrated magnetically geared machines have generated significant interest over the past twenty years [9]-[13], and other researchers have developed prototypes for wind [14], [15] and wave [16] energy harvesting, commercial air compressors [17], robotics [18], traction [19], [20], and hybrid electric vehicle power split devices [21].

Most existing magnetic gear literature [6]-[21] focuses on coaxial magnetic gears, such as the one in Fig. 1(a), which perform best at relatively low gear ratios, often less than 10:1 [22]. However, electric aviation propulsion, aerospace actuation, robotics, and space applications often require high specific torques at high gear ratios [5], [23]. Cycloidal magnetic gears, such as the one illustrated in Fig. 1(b), can achieve much higher specific torques than coaxial magnetic gears at higher gear ratios [24]. In magnetic cycloidal gears, the non-uniform, time-varying air gap creates permeance harmonics, which modulate the fields from the rotors [25]. Since the air gap's fundamental permeance spatial harmonic is unity, the number of
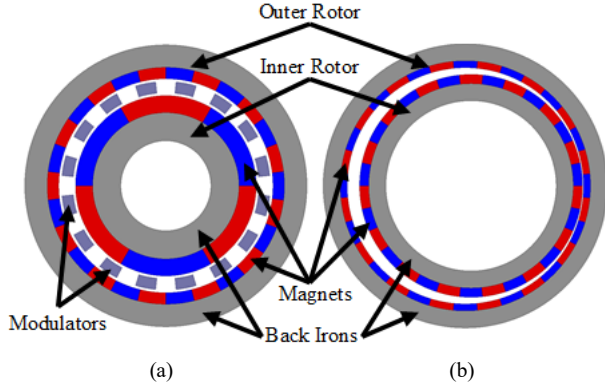
Fig. 1. (a) Coaxial and (b) cycloidal radial flux magnetic gears with surface permanent magnets [24].

inner (P_{In}) and outer (P_{Out}) rotor pole pairs should be related by

$$P_{Out} = P_{In} + 1 \qquad (1)$$

for optimal operation, as indicated in [26]. The most practical operating configuration that yields a high gearing ratio is obtained by keeping the outer rotor stationary and connecting the inner rotor's rotation about its own axis to the low-speed shaft and the inner rotor's orbital motion about the outer rotor's axis to the high-speed shaft. This yields the gear ratio given by

$$G = \frac{\omega_{Orb}}{\omega_{Rot,In}} = -P_{In}, \qquad (2)$$

where ω_{Orb} is the speed of the inner rotor's orbital revolution about the outer rotor's axis and $\omega_{Rot,In}$ is the speed of the inner
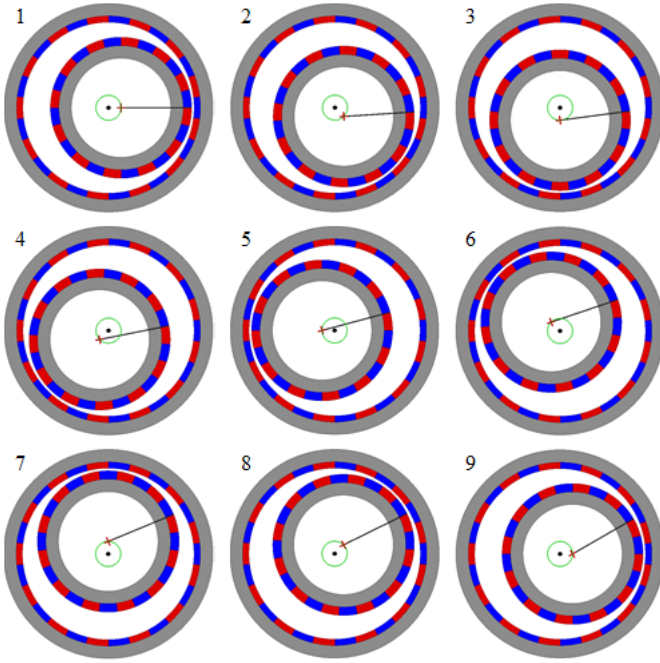

Fig. 2. Example cycloidal magnetic gear operation motion sequence. The inner rotor's axis (red '+') orbits the outer rotor's axis (black dot) along the green path while the inner rotor rotates about its own axis [24].
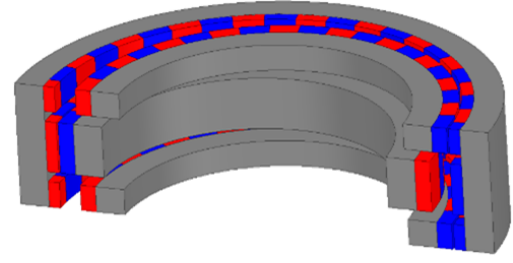

Fig. 3. Example radial flux cycloidal magnetic gear with three mechanically phase-shifted rotor segments to balance the center of mass, radial magnetic forces, and the off-axis moment created by the radial magnetic forces.

rotor's rotation about its own axis. The negative sign in (2) indicates that the shafts will rotate in opposite directions. This operation is illustrated in Fig. 2. The gear in Fig. 2 uses 12 inner pole pairs; therefore, for each step in Fig. 2, the inner rotor rotates 3.75° counterclockwise about its own axis, while its own axis orbits 45° clockwise about the outer rotor's axis [24].

Like Nabtesco's [27], NIDEC-SHIMPO's [28], and Sumitomo's [29] commercial precision mechanical cycloidal gearboxes, some previous cycloidal magnetic gear prototypes used two mechanically phase-shifted inner rotors to balance the center of mass about the axis of rotation and mitigate the vibrations associated with the inner rotor's eccentric motion [26], [30]. However, unlike their mechanical counterparts, cycloidal magnetic gears have a significant radial force component, which decreases monotonically as the load angle increases [31], [32]. While the multi-rotor solutions proposed in [26], [30], [31], [33] balance both the center of mass and the radial magnetic forces, the radial forces create an off-axis torque. The cycloidal magnetic gear prototype described in this paper is the first described in the literature to use more than two rotor segments to balance the off-axis moment in addition to the center of mass and the radial magnetic forces. Specifically, as illustrated in Fig. 3, the cycloidal magnetic gear prototype described in this paper uses a tripartite inner and outer rotors consisting of a first rotor segment accounting for a quarter of the total active stack length, a middle rotor segment accounting for half of the total active stack length, and a third rotor segment accounting for the last quarter of the total active stack length. The middle rotor segment is rotated 180° about the outer rotor's axis relative to the other rotor segments to balance out the net radial forces on the rotor and maintain a constant center of mass.

Recent literature contains parametric analyses of cycloidal magnetic gears with conventional [24], Halbach [31], and flux-focusing magnet arrangements [33] and a few proof-of-concept prototypes [25], [26], [32], [34]. The design analysis presented in this paper builds upon previous optimization studies [24], [31], [33] by accounting for manufacturing considerations, and the results reveal that the optimum magnetic design parameters change significantly when these critical details are considered. Specifically, this paper employs an extensive parametric 2-D electromagnetic finite element analysis (FEA) study to optimize the design of a high-gear-ratio cycloidal magnetic gear that will serve as the high-torque stage in a multistage magnetic gear train with a total gear ratio of 1000:1. 3-D FEA predictions are compared with experimental results, which reveal that the gear's specific torque is competitive with those of commercial cycloidal mechanical drives.

II. DESIGN STUDY METHODOLOGY

This paper uses an extensive parametric 2-D electromagnetic FEA study to characterize optimum design trends for a surface permanent magnet (SPM) cycloidal magnetic gear subject to practical manufacturing constraints. Table I summarizes the various design parameters and associated values considered. All feasible parameter value design combinations in Table I were simulated using 2-D FEA. In all designs, the inner and outer rotor back irons were set to the same radial thickness, T_{BI}, and the inner and outer rotor permanent magnets (PMs) were also set to the same radial thickness, T_{PM}. This was done to reduce the parametric design space's dimensionality and the simulation case count, but it is expected that the two back irons and two sets of PMs will each exhibit similar optimum thicknesses because the two rotors have similar pole counts and radii.

Due to the high pole count of optimal cycloidal magnetic gear designs, the magnets tended to have a small arc length and the tolerance controls required to successfully implement an SPM cycloidal magnetic gear were infeasible. Thus, small ribs ($T_R > 0$) or ruts ($T_R < 0$) between magnets were evaluated as means of facilitating magnet placement, as shown in Fig. 4. Compared to NdFeB, SmCo type PMs are more tolerant of radiation [35] and retain their magnetic properties at lower cryogenic temperatures [36]-[37]; therefore, they will likely be used for higher technology readiness level (TRL) prototypes. However, for the proof-of-concept prototype, N52H was available, and thus in all simulated designs, the back irons and PMs are made from M15 steel and NdFeB N52H, respectively. Mass is critical for space applications; therefore, specific torque (a gear's slip torque divided by its mass) is used as the primary design metric. This paper's simulation results are based on active mass (the mass of the PMs and electrical steel).

III. ELECTROMAGNETIC SIMULATION RESULTS

A. Design for Manufacturing and Assembly Tradeoff Analysis

Fig. 5 shows the active specific torques that the cycloidal magnetic gear can achieve at different gear ratios and outer radii and with different practical fabrication constraints. The blue lines in Fig. 5 indicate the maximum achievable specific torque at each gear ratio and outer radius combination, when no ribs or ruts are used and no back iron constraints are imposed. The reasons for these trends are explained in [24], [31], [33], and the trends predominantly leads to air core ($T_{BI} = 0$ mm) designs. Figs. 6(a)-6(c) correspond to the solid blue line in Fig. 5 and demonstrate the variation of the maximum achievable specific torque with gear ratio, back iron thickness, PM thickness, and axis offset at a 100 mm outer radius. Thus, Figs. 6(a) and 6(b) indicate that, within the evaluated design space, thinner back irons and thinner magnets enable higher specific torques and shift the optimal gear ratios higher. Similarly, Fig. 6(c) shows that decreasing the axis offset increases the optimal gear ratio; however, within the evaluated design space, there is a non-trivial axis offset (of 1.5 mm to 2 mm), which maximizes the specific torque. Although air core designs yield high active specific torques, they are more difficult to assemble because the magnets are not attracted to a back iron. Additionally, designs without ribs or ruts to position the magnets are more difficult to assemble and susceptible to tolerance stack up. Consequently, at least

TABLE I. PARAMETER SWEEP RANGES

Parameter	Values	Units
Inner pole pair count (P_{In})	30, 32, … 60	
Outer radius (R_{Out})	50, 75, 100	mm
Back iron thickness (T_{BI})	0ᵃ, 2, 3, 4, 5	mm
PM Thickness (T_{PM})	2, 3, 4, 5	mm
Minimum air gap thickness (T_{AG})	1	mm
Axis offset (T_{Off})	0.5, 1, 2, 3, 4	mm
Back iron rib or rut thickness (T_R)	–1, 0, 1, 2	mm
Back iron rib or rut width (W_R)	0, 1, 2	mm
Torque angle (θ_T)	0, 90	degrees

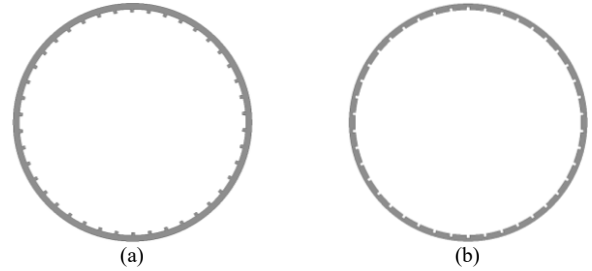a. Refers to air core designs, wherein magnets are held by a nonmagnetic structural material.

Fig. 4. Outer rotor back irons with (a) 1 mm by 1 mm ribs ($T_R > 0$) and (b) 1 mm by 1 mm ruts ($T_R < 0$)

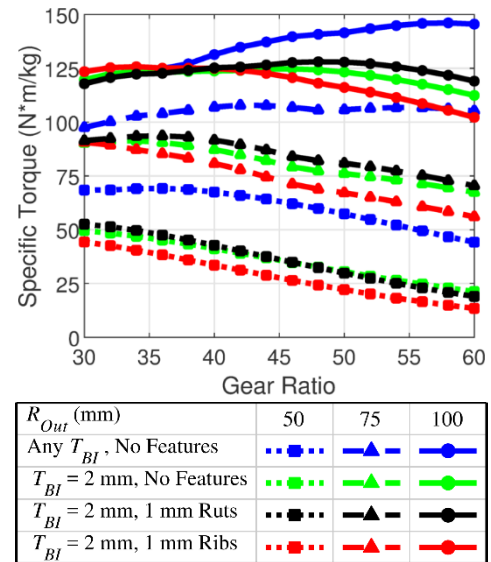| R_{Out} (mm)	50	75	100
Any T_{BI}, No Features	▪▪▪	▲—	●—
T_{BI} = 2 mm, No Features	▪▪▪	▲—	●—
T_{BI} = 2 mm, 1 mm Ruts	▪▪▪	▲—	●—
T_{BI} = 2 mm, 1 mm Ribs	▪▪▪	▲—	●—

Fig. 5. Variation of the maximum active specific torque with gear ratio and outer radius under different levels of practical fabrication constraints.

2 mm thick back irons were considered, and 1 mm by 1 mm ribs or ruts were studied for magnet location. The green, red, and black lines in Fig. 5 demonstrate how imposing these practical fabrication considerations reduces the achievable specific torque and decreases the gear ratio corresponding to the maximum achievable specific torque. The prototype has 2.5 mm thick back irons and 1 mm by 1 mm ruts between the magnets. Figs. 6(e)-6(g) and Figs. 6(i)-6(k) demonstrate how considering practical constraints, such as ribs (Figs. 6(e)-6(g)), decreases the optimal gear ratio at different PM thickness and axis offset values. The deleterious impact of using the ribs increases with
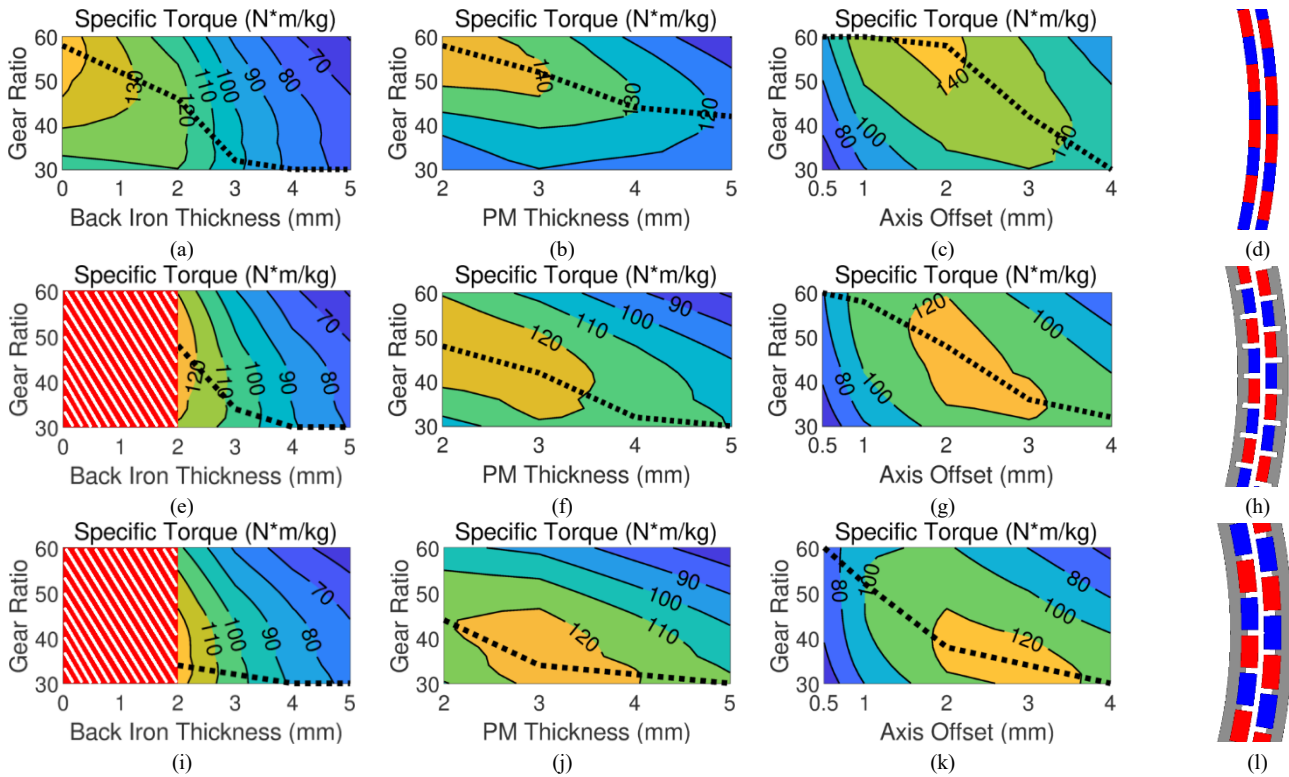
Fig. 6 Variation of the maximum active specific torque with gear ratio, (a) back iron thickness, (b) PM thickness, and (c) axis offset under no practical fabrication constraints at $R_{Out} = 100$ mm. Variation of the maximum active specific torque with gear ratio, (e) back iron thickness, (f) PM thickness, and (g) axis offset when ruts ($T_R = -1$ mm, $W_R = 1$ mm) are used between the PMs and the back iron is required to be at least 2 mm thick at $R_{Out} = 100$ mm. Variation of the maximum active specific torque with gear ratio, (i) back iron thickness, (j) PM thickness, and (k) axis offset when ribs ($T_R = 1$ mm, $W_R = 1$ mm) are used between PMs and the back iron is required to be at least 2 mm thick at $R_{Out} = 100$ mm. The dashed black lines trace the gear ratio maximizing the specific torque at each x-axis value. A portion of the cross section of the designs which optimize specific torque for the three cases characterized above are shown in (d), (h), and (l).

the gear ratio because ribs of a fixed width (such as 1 mm) consume a bigger percentage of the pole arc as the gear ratio (pole count) increases and the pole arc decreases. The black lines in Fig. 5 suggest a higher optimal gear ratio for designs with ruts; however, this may be misleading as nonmagnetic spacers must be used for magnet location, which will ultimately increase the total mass. Figs. 6(d), 6(h), and 6(l) show a section of the geometry of the magnetically optimal designs for the unconstrained case, and the cases constrained to have a 2 mm thick back iron and 1 mm by 1 mm ruts or ribs, respectively. Thus, using ribs lowers the optimal gear ratio (pole count) so that the ribs eliminate less PM material. Given such radially thin magnets, the ribs cause significant flux shorting; consequently, the optimal design with ribs requires thicker magnets, as shown in Fig. 6(l). The final prototype parameters are listed in Table II. The rated high-torque output speed is 1 rpm.

B. Radial Force Analysis

The maximum radial forces on the inner rotor occur at a 0° torque angle and monotonically decrease as the load angle increases. However, tangential forces on the rotor increase as the load angle increases [31], [32]. Fig. 7(a) reveals that, at the same outer radius, the maximum radial force experienced by designs optimized for specific torque decreases as the axis offset increases and pole count increases. This is because, as axis offset decreases, some repulsive forces from the magnets in the region with the large air gap become more significant. Fig. 7(b)

TABLE II. PROTOTYPE ACTIVE DESIGN PARAMETER VALUES

Parameter	Values	Units
Outer Back Iron Outer Diameter[a]	201	
Outer Back Iron Radial Thickness[a, b]	2.5	mm
Inner and Outer Magnet Radial Thicknesses	2.5	mm
Minimum Air Gap Thickness	1.5	mm
Axis Offset	1.75	mm
Inner Rotor Back Iron Radial Thickness	3	mm
Axial Spacing Between Rotor Segments	6.5	mm
Total Active Stack Length	45.4	mm

[a] Not including additional thickness to allow for structural through-holes on corners of back iron
[b] 1 mm by 1 mm ruts are notched into the back irons between every magnet piece as shown in Fig. 4(b)
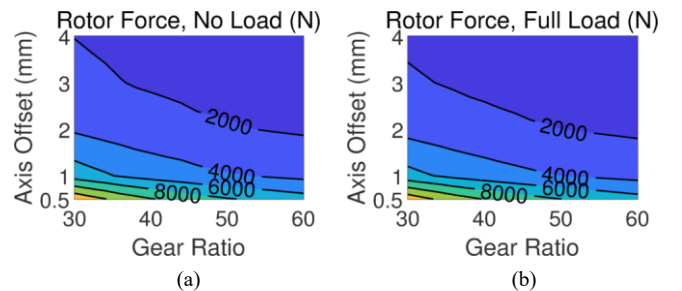

Fig. 7 (a) Maximum forces at no load ($\theta_T = 0°$) and (b) at full load ($\theta_T = 90°$) angle, corresponding to optimal designs with no ribs or ruts or back iron constraints at $R_{Out} = 100$ mm.
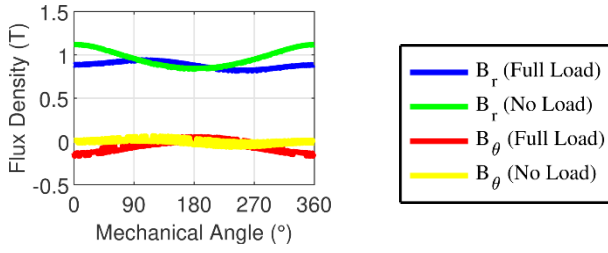
Fig. 8 Radial and tangential flux densities predicted by FEA in the center of a selected outer rotor magnet over a full mechanical cycle for the prototype gear with the parameter values listed in Table II.

shows the force on the inner rotor at the full load angle. The net magnetic forces on the rotor at full load and no load are similar.

C. Transient Analysis

A transient analysis of the prototype at rated speed and power indicated that it can achieve greater than 99% electromagnetic efficiency at full load. Additionally, the electromagnetic simulations of the prototype exhibit less than 1% peak-to-peak torque ripple in steady state operation. These results agree with the findings in [33]. Previous authors attributed the low electromagnetic losses to the low input speed and the high segmentation of the magnetically active and conductive components [33]. Fig. 8 reveals an additional reason for the relatively low electromagnetic losses of the gear; the radial and tangential flux density components in a magnet do not change significantly over an orbital cycle.

IV. STRUCTURAL ANALYSIS

A. Reaction Force and Internal Stress Distribution Analysis

In a mechanical cycloidal gear, slightly less than half of the teeth interact with the external rollers to transfer positive torque, while the other external pins transfer no torque [38]-[40]. However, as revealed in [24], in a loaded cycloidal magnetic

gear, all magnets experience tangential forces, some of which oppose each other. Compared to its mechanical analog, a magnetic cycloidal gear will experience higher reaction forces on its internal pins and central eccentric bearing due to the previously discussed large radial forces [24], [31], [32]. Additionally, the internal stress distribution inside the structure of the cycloidal magnetic gear will differ significantly from that inside of a cycloidal mechanical gear.

Assuming perfectly-toleranced geometries and perfectly rigid bodies, the central eccentric bearing bears the radial load at the zero torque (no-load) orientation. As the load increases, the tangential forces on the magnets monotonically increase, and the radial forces on the magnets monotonically decrease, but not to zero [32]. The moment produced on the inner rotor by these tangential forces is transferred to the output shaft, which is coaxial with the input shaft, via the straight-line mechanism principle, wherein the cycloidal disc collaborates with internal pins extending from the output shaft. Assuming all m internal pins collaborate with the cycloidal disc with negligible friction, only compression forces can be transferred to the internal pins by the cycloidal disc [38]-[40]. Assuming the back iron and cycloidal disc are one body, the extended free-body-diagram (FBD) in Fig. 9(a) illustrates the rigid body static equilibrium and previously discussed straight-line mechanism. While the red and blue vectors are scaled correctly relative to each other, and for the same color the vector scaling is proper, the vectors are generally not to scale across colors to enhance readability of the FBD. The static force equilibrium can be written as

$$\sum_{j=1}^{m} \boldsymbol{Q}_j + \boldsymbol{F} = \sum_{i=1}^{2nP_1} \boldsymbol{P}_i \quad , \qquad (3)$$

where $\boldsymbol{Q}_j$ is the reaction force vector acting on the jth internal pin, $\boldsymbol{F}$ is the reaction force vector of the central eccentric bearing, $\boldsymbol{P}_i$ is the magnetic force vector acting on the ith inner rotor magnet,
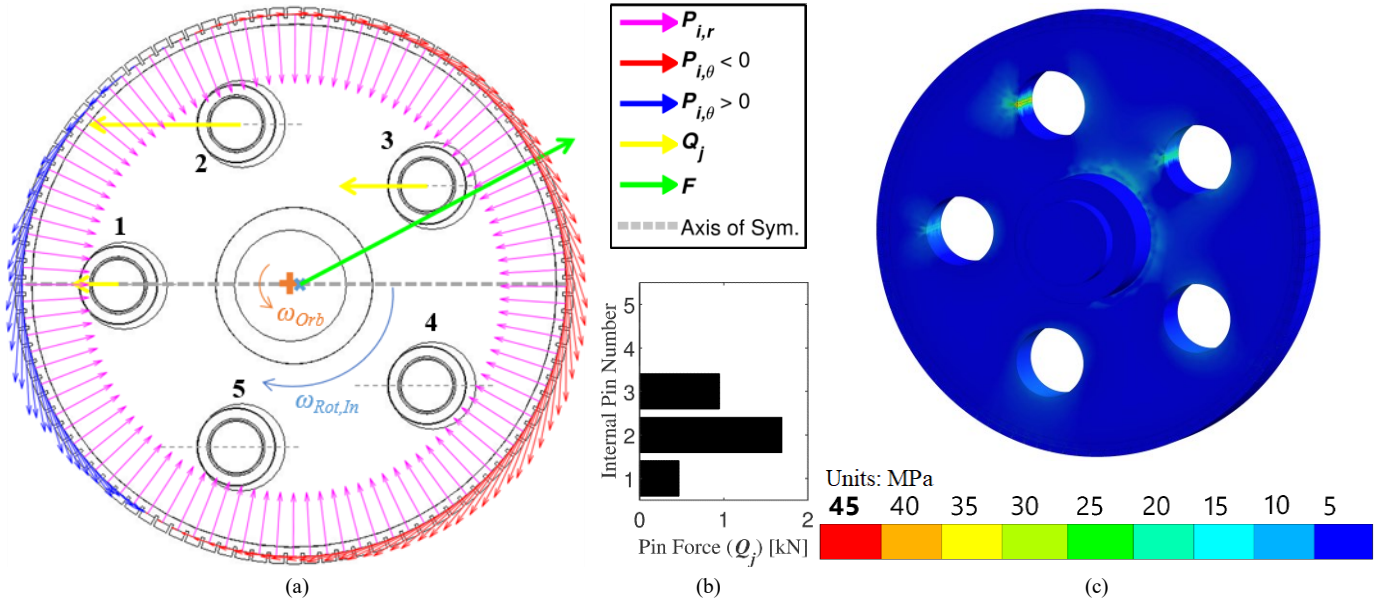

(a)   (b)   (c)

Fig. 9 (a) Extended free-body diagram showing magnet radial ($\boldsymbol{P}_{i,r}$) and tangential ($\boldsymbol{P}_{i,\theta}$) force vector components and internal pin ($\boldsymbol{Q}_j$) and central eccentric bearing ($\boldsymbol{F}$) reaction force vectors acting on an example solid cycloidal disc. (b) Pin reaction forces and (c) the corresponding Von-Mises stress distribution predicted by ANSYS Static Structural for this non-optimized example inner rotor with a solid-steel cycloidal disc.

and n is the number of magnet pieces per pole. Even with the prior assumptions, the reaction forces on the internal pins and the bearing reaction forces are statically indeterminate. To solve the system without consideration of elastic compliance, previous authors have made questionable assumptions about the reaction force distribution [38]-[40].

To obtain P_i, a 2-D discretized cycloidal magnetic gear model was created, wherein each magnet was an object with its own coordinate system, and the radial and tangential force components on the ith magnet were obtained at the full load (slip torque) angle. After assigning proper boundary conditions, the radial and tangential forces of each magnet were mapped directly to the ANSYS Static Structural FEA simulation tool. Fig. 9(b) below shows the resulting internal pin reaction forces (Q_j) for a design magnetically similar to that of the half-rotor stack of the 50:1 prototype, with parameters shown in Table II. The resulting analysis reveals a significant force on the central eccentric bearing. Fig. 9(c) shows the stress distribution inside this example solid steel cycloidal disc with 5 circulation holes. It is evident from Fig. 9(c) that this example cycloidal disc is heavily over-engineered. However, having an accurate model of the internal stress distribution enables topology optimization to significantly reduce the structural weight of the cycloidal disc. Substantial portions of the cycloidal disc and faceplate mass were eliminated for the developed proof-of-concept prototype.

B. Analytical Mechanical Bearing Loss Analysis

Cycloidal magnetic gears, like their mechanical counterparts, require numerous bearings, each of which is subject to large time-varying forces. The total losses (P_{loss}) in a cycloidal magnetic gear can be written as

$$P_{loss} = P_{EM} + P_{B,Pins} + P_{B,Input} + P_{B,Output}, \quad (4)$$

where P_{EM} is the total power loss of electromagnetic origin, $P_{B,Pins}$ is the total power loss associated with all of the internal pins' bearings, and $P_{B,Input}$ and $P_{B,Output}$ are the total power losses in the bearings on the input and output shafts, respectively. Losses in the input and output shaft seals will be considered negligible for the cycloidal magnetic gear. Mechanical cycloidal gears have additional losses in the cooperation areas of external pins, bushings, and the cycloidal disc, as well as hydraulic power losses due to oil mixing resistance and squeezing loss in the areas of tooth rolling contact [38]. It should be noted that magnetic gearing technology does not address the tribological challenges associated with bearings in dusty and extremely cold environments. The proof-of-concept (POC) prototype discussed in this paper uses commercial-off-the-shelf bearings and was designed for room-temperature operation.

P_{EM}, the total power loss of electromagnetic origin, includes the losses in the electrical steel and magnets discussed earlier, as well as any eddy current losses which may be produced in housing and internal structural materials. In the POC prototype design, sufficient axial buffer space was provided between the magnetically active stack and the aluminum housing to avoid inducing significant eddy current losses in the structural material, a problem that has severely impacted the efficiencies of previous prototype magnetic gears, as in [41].

Assuming the bearing working temperature to be 40°C [38], and given the axial pre-loading, rotational velocity of each bearing external raceway, oil viscosity at the working temperature, and oil level, [42] can be used to approximate $P_{B,Input}$ and $P_{B,Output}$. The input and output bearing losses at rated power and speed are approximated to be 0.011 W.

The power loss associated with the jth internal pin ($P_{B,Pins,j}$) is comprised of two components: the rolling cooperation of the cycloidal disc on the bearing of that internal pin and the sliding cooperation of the same bearing on its internal pin. Hence, as in [38], the total power loss associated with all internal pins is

$$P_{B,Pins} = \sum_{j=1}^{m} Q_j \left(r_{sleeve} \mu_{roll} \omega_{sleeve} + r_{pin} \mu_{slide} \omega_{Orb} \right) \quad (5)$$

where r_{sleeve} and r_{pin} are the outer radius of the internal pin's sleeve bearing and the internal pin itself, μ_{roll} and μ_{slide} are the coefficients of rolling friction and sliding friction, which are determined from previous experimental data [38], and ω_{sleeve} is the angular velocity of the internal pin sleeve. At rated power and speed, using the results shown in Fig. 9(b) and the geometry of the design, the total internal pin bearing losses are estimated using (5) to be at least 8 W.

Based on (4), and the rated input power of 18 W, the analysis suggests that the prototype will achieve an efficiency of 56% for continuous operation at rated torque and speed. The true values of μ_{roll} and μ_{slide}, as well as manufacturing tolerances will affect the estimated efficiency. The authors have already developed revised bearing solutions that are expected to drastically increase the efficiency of future prototypes. Previous researchers observed full-load efficiencies ranging from 92% to 94%, and observed that for the same torque, efficiency decreased as speed increased [26]; thus, it is possible to achieve much higher efficiencies with cycloidal magnetic gears.

V. EXPERIMENTAL PROOF-OF-CONCEPT PROTOTYPE

Table II shows the active design parameter values for the magnetically optimized 50:1 cycloidal magnetic gear prototype. Fig. 10 shows the POC prototype gear with a plexiglass face

Fig. 10 The 50:1 tripartite rotor cycloidal magnetic gear POC prototype.

TABLE III.   Simulated & Experimentally Measured Slip Torque

Measurement	3-D FEA Result	Experimental Result
Slip Torque[a]	193.84 N·m	171.8 N·m
Specific Torque[b]	—	17.2 N·m/kg

[a]Locked high speed input shaft.
[b]Mass includes input and output shafts.

plate. Table III compares experimental torque measurements and specific torque calculations with 3-D FEA torque predictions. Specific torque measurements include the input and output shaft masses.

The 50:1 cycloidal magnetic gear used keyways on the tripartite rotor segments to mate with keys on the input cam shaft in an attempt to ensure each consecutive rotor segment remained magnetically in phase after being eccentrically mounted 180° mechanically out of phase. Given that there are 100 poles on the inner rotor, a pole arc is only 3.6°. During assembly, it was observed that the rotors were not perfectly mounted on the keys, and a small angular misalignment may exist between each consecutive rotor. Fig. 11 illustrates the impact of small angular misalignments between the quarter stack length rotor segments (the first and third rotor segments) and the middle, half stack length rotor segment. This analysis reveals that an approximately 1° mechanical angular misalignment between one of the quarter stack length rotor segments and the half stack length rotor segment could account for the discrepancy between the 193.84 N·m slip torque predicted by the 3-D FEA model and the experimentally measured 171.8 N·m experimentally measured slip torque. Additionally, this discrepancy is likely not a result of any issues with the simulation model, as the slip torque prediction by a similar model for the 20:1 stage in the series gear train achieved a 95.1% match with the experimentally measured value for a prototype of that stage.

The POC prototype possesses several non-optimal structural design features. For example, the input and output shafts are made of solid steel due to limited time and cost considerations. Hollow input and output shafts made of titanium could be employed, while still maintaining a safety factor acceptable to aerospace standards, to increase the specific torque of the 50:1 gear to 20.5 N·m/kg. Nevertheless, the specific torques of these sub-optimal prototypes are competitive with those of commercial Nabtesco RDS series models, as shown in Fig. 12. Fig. 12 reveals that the specific torques of cycloidal magnetic
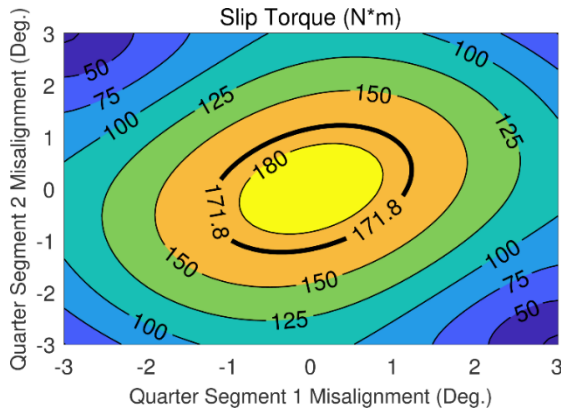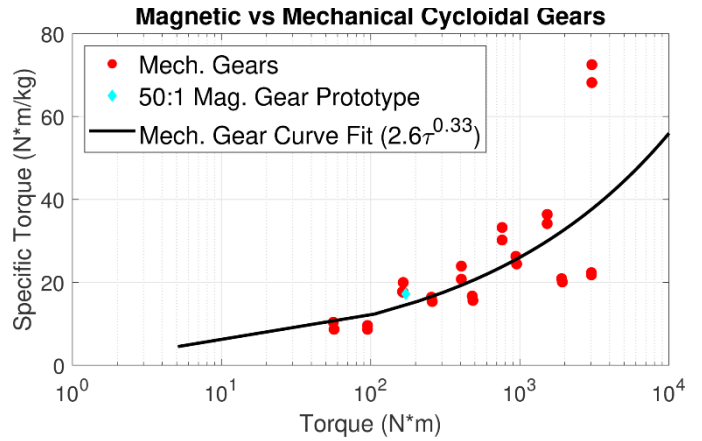
Fig. 12 Comparison of specific torques for the 50:1 cycloidal magnetic gear prototype (based on total mass) and models from the Nabtesco RDS series [23]. The black line indicates a curve fit of the specific torques of the Nabtesco RDS series models.

gears may be capable of surpassing those of their mechanical counterparts. Further study is needed to determine how the efficiency and reliability of more optimal cycloidal magnetic gears compare to the efficiency and reliability of cycloidal mechanical gears.

VI. Conclusion

This manuscript contributes a practical perspective on cycloidal magnetic gears to the literature.

- A three-segment rotor, shown in Fig. 3, is proposed to simultaneously balance the off-axis moment on the shaft, as well as the center of mass and the radial magnetic forces.
- However, Fig. 11 demonstrates that the slip torque of the three-segment rotor is very sensitive to small misalignments between rotors.
- Figs. 5 and 6 illustrate the significant impacts of considering fabrication constraints, such as a minimum back iron thickness and ribs or ruts (depicted in Fig. 4) for magnet positioning, on the optimization process.
- A discretized model of the SPM cycloidal magnetic gear is used to accurately model the internal pin reaction forces and the stress distribution in the cycloidal disc, as demonstrated in Fig. 9.
- An approach for evaluating mechanical losses in the cycloidal magnetic gear, which dominate the electromagnetic losses, is presented.
- The cycloidal magnetic gear prototype shown in Fig. 10 was developed and its experimental results are compared with the simulation results in Table III.
- Fig. 12 reveals that the specific torque of the POC cycloidal magnetic gear prototype is already highly competitive with those of its technologically-mature commercial mechanical counterparts. Nonetheless, simple changes, such as using hollow shafts, could drastically reduce the cycloidal magnetic gear's structural mass and increase its specific torque.

Fig. 11 The effects of imprecise phase-shifting between the rotor segments.

REFERENCES

[1] J. Zakrajsek *et al.*, "Exploration rover concepts and development challenges," NASA Glenn Res. Center, Cleveland, OH, USA, Tech. Rep. TM—2005-213555, Mar. 2005.

[2] Boeing Co., "Apollo 17 LRV technical information," Apollo Lunar Surface J., 1972. [Online]. Available: https://www.hq.nasa.gov/alsj/alsj-LRVdocs.html

[3] R. G. Bonitz, T. T. Nguyen and W. S. Kim, "The Mars Surveyor '01 rover and robotic arm," in *Proc. IEEE Aero. Conf.*, 2000, pp. 235-246.

[4] J. D. Smith, A. J. Nick, J. M. Schuler, A. Kennett and R. P. Dillon, "Cryobotics: extreme cold environment testing of strain wave gear sets," in *Proc. IEEE Aero. Conf.*, 2019, p. 1-10.

[5] G. Puchhammer, "Magnetic gearing versus conventional gearing in actuators for aerospace applications," in *Proc. Aero. Mech. Symp.*, 2014, pp. 175-181.

[6] T. F. Tallerico, Z. A. Cameron, J. J. Scheidler and H. Hasseeb, "Outer stator magnetically-geared motors for electrified urban air mobility vehicles," in *Proc. AIAA/IEEE Elect. Aircraft Technol. Symp.*, 2020, pp. 1-25.

[7] J. Esnoz-Larraya *et al.*, "OPTIMAGDRIVE: high-performance magnetic gears development for space applications," in *Proc. European Space Mechanisms and Tribology Symp.*, 2017.

[8] J. L. Perez-Diaz *et al.*, "Performance of magnetic-superconductor non-contact harmonic drive for cryogenic space applications," *Machines*, vol. 3, no. 3, pp. 138-156, 2015.

[9] K. Atallah and D. Howe, "A novel high-performance magnetic gear," *IEEE Trans. Magn.*, vol. 37, no. 4, pp. 2844–2846, Jul. 2001.

[10] P. O. Rasmussen, T. O. Anderson, F. T. Jorgensen, and O. Nielsen, "Development of a high performance magnetic gear," *IEEE Trans. Ind. Appl.*, vol. 41, no. 3, pp. 764–770, May/Jun. 2005.

[11] P. M. Tlali, R-J. Wang, and S. Gerber, "Magnetic gear technologies: A review," in *Proc. Int. Conf. Elect. Mach.*, 2014, pp. 544–550.

[12] B. Praslicka, M. C. Gardner, M. Johnson and H. A. Toliyat, "Review and analysis of coaxial magnetic gear pole pair count selection effects*," IEEE J. Emerg. Sel. Topics Power Electron.*, early access. doi: 10.1109/JESTPE.2021.3053544.

[13] Z. Q. Zhu, H. Y. Li, R. Deodhar, A. Pride and T. Sasaki, "Recent developments and comparative study of magnetically geared machines," in *CES Trans. Elect. Mach. and Sys.*, vol. 2, no. 1, pp. 13-22, March 2018.

[14] K. Li, S. Modaresahmadi, W. B. Williams, J. D. Wright, D. Som and J. Z. Bird, "Designing and experimentally testing a magnetic gearbox for a wind turbine demonstrator," *IEEE Trans. Ind. Appl.*, vol. 55, no. 4, pp. 3522-3533, Jul.-Aug. 2019.

[15] A. B. Kjaer, S. Korsgaard, S. S. Nielsen, L. Demsa and P. O. Rasmussen, "Design, fabrication, test, and benchmark of a magnetically geared permanent magnet generator for wind power generation," *IEEE Trans. Energy Conv.*, vol. 35, no. 1, pp. 24-32, Mar. 2020.

[16] M. Johnson, M. C. Gardner, H. A. Toliyat, S. Englebretson, W. Ouyang, and C. Tschida, "Design, construction, and analysis of a large scale inner stator radial flux magnetically geared generator for wave energy conversion," *IEEE Trans. Ind. Appl.*, vol. 54, no. 4, pp. 3305–3314, Jul./Aug. 2018.

[17] A. Matthee, R. Wang, C. Agenbach, D. Els, M. Kamper, "Evaluation of a magnetic gear for air-cooled condenser applications," *IET Electr. Power. Appl.*, vol. 12, no. 5, pp. 677-683, Apr. 2018.

[18] R. Zanis, A. Borisavljevic, J. W. Jansen and E. A. Lomonova, "Modeling, design and experimental validation of a small-sized magnetic gear," in *Proc. Int. Conf. Elec. Mach. and Sys.*, 2013, pp. 560-565

[19] P. O. Rasmussen, T. V. Frandsen, K. K. Jensen and K. Jessen, "Experimental evaluation of a motor-integrated permanent-magnet gear," *IEEE Trans. Ind. Appl.*, vol. 49, no. 2, pp. 850-859, March-April 2013.

[20] T. V. Frandsen *et al.*, "Motor integrated permanent magnet gear in a battery electrical vehicle," *IEEE Trans. Ind. Appl.*, vol. 51, no. 2, pp. 1516-1525, Mar.-Apr. 2015.

[21] P. Chmelicek, S. D. Calverley, R. S. Dragan and K. Atallah, "Dual rotor magnetically geared power split device for hybrid electric vehicles," *IEEE Trans. Ind. Appl.*, vol. 55, no. 2, pp. 1484-1494, Mar.-Apr. 2019.

[22] M. C. Gardner, M. Johnson, and H. A. Toliyat, "Analysis of high gear ratio capabilities for single-stage, series multistage, and compound differential coaxial magnetic gears," *IEEE Trans. Energy Convers.*, vol. 34, no. 2, pp. 665-672, Jun. 2019.

[23] Motus Labs, Dallas, TX, USA, "Torque density consequences for robot arm design," Aug. 8, 2018. [Online]. Available: https://motus-labs.com/torque-density-consequences-for-robot-arm-design-2/

[24] M. C. Gardner, M. Johnson, and H. A. Toliyat, "Comparison of surface permanent magnet coaxial and cycloidal radial flux magnetic gears," in *Proc. IEEE Energy Convers. Congr. and Expo.*, 2018, pp. 5005-5012.

[25] J. Rens, K. Atallah, S. D. Calverley, and D. Howe, "A novel magnetic harmonic gear," *IEEE Trans. Ind. Appl.*, vol. 46, no. 1, pp. 206-212, Jan./Feb. 2010.

[26] F. Jørgensen, T. Andersen and P. Rasmussen, "The cycloid permanent magnetic gear," *IEEE Trans. Ind. Appl.*, vol. 44, no. 6, pp. 1659-1665, Nov.-Dec. 2008.

[27] https://www.nabtescomotioncontrol.com/

[28] http://www.drives.nidec-shimpo.com/en/erh-series-cycloidal-reducer/

[29] https://us.sumitomodrive.com/en/cyclo-gear-drives

[30] T. Andersen and F. Jørgensen,, "Magnetic device for transfer of forces," World Patent WO 2006/133703 A1, Dec. 21, 2006.

[31] H. Huang, R. Qu and J. Bird, "Performance of Halbach cycloidal magnetic gears with respect to torque density and gear ratio," in *Proc. IEEE Int. Elect. Mach. Drives Conf.*, 2019, pp. 1977-1984.

[32] K. Davey, T. Hutson, L. McDonald and G. Hutson, "The design and construction of cycloidal magnetic gears," in *Proc. IEEE Int. Elect. Mach. Drives Conf.*, 2017, pp. 1-6.

[33] K. Li, J. Bird, J. Kadel and W. Williams, "A flux-focusing cycloidal magnetic gearbox," *IEEE Trans. Magn.*, vol. 51, no. 11, pp. 1-4, Nov. 2015.

[34] K. Davey, L. McDonald and T. Hutson, "Axial flux cycloidal magnetic gears," *IEEE Trans. Magn.*, vol. 50, no. 4, pp. 1-7, April 2014.

[35] J. L. Mesa *et al.*, "Effects of γ-ray radiation on magnetic properties of NdFeB and SmCo permanent magnets for space applications," in *Proc. IEEE Radiation Effects Data Workshop*, 2014, pp. 1-4, doi: 10.1109/REDW.2014.7004566.

[36] Arnold Magnetic Technologies, "Using permanent magnets at low temperature", TN 0302 rev.2015a, Rochester, NY, USA.

[37] Arnold Magnetic Technologies , "Temperature effects on magnetic output", TN 0303 rev.2015a, Rochester, NY, USA.

[38] K Olejarczyk, M Wikło and K Kołodziejczyk, "The cycloidal gearbox efficiency for different types of bearings—Sleeves vs. needle bearings," *J. Mech. Eng. Sci.*, vol. 233, no. 21-22, pp. 7401-7411, Jun. 2019.

[39] C. Gorla *et al*. "Theoretical and Experimental Analysis of a Cycloidal Speed Reducer". *J. Mech. Design*, vol. 130, no. 11, pp. 1–8, 2008.

[40] S. K. Malhotra, M. A. Parameswaran, "Analysis of a cycloid speed reducer". *Mechanism Mach. Theory*, vol. 18, no. 6, pp. 491–499, 1983.

[41] K. Li, S. Modaresahmadi, W. B. Williams, J. Z. Bird, J. D. Wright and D. Barnett, "Electromagnetic analysis and experimental testing of a flux focusing wind turbine magnetic gearbox," ," *IEEE Trans. Energy Convers.*, vol. 34, no. 3, pp. 1512-1521, Sept. 2019.

[42] AB SKF, Gothenburg, Sweden, "SKF Bearing Select", Version 1.2.93. [Online]. Available: https://www.skf.com/us/support/engineering-tools/bearing-select